Electronic Supplementary Material (ESI) for CrystEngComm.

Supporting Information

Coordination compound-derived La-doped FeS_2/N-doped carbon (NC) as an efficient electrocatalyst for oxygen evolution reaction

Xuan Ao Ma, Yang Hai and Yun Gong*

Department of Applied Chemistry, College of Chemistry and Chemical Engineering, Chongqing University, Chongqing 401331, P. R. China Tel: +86-023-65678932 E-mail: gongyun7211@cqu.edu.cn

S1 Experimental

S1.1 Materials

Lanthanum nitrate hydrate [$La(NO_3)_3 \cdot 6H_2O$], ferric nitrate hydrate [$Fe(NO_3)_3 \cdot 9H_2O$], potassium ferricyanide {$K_3[Fe(CN)_6]$}, hexamethylenetetramine (hmt), sulfur (S), potassium hydroxide (KOH), ethanol (99.5%) used in the experiment were of analytical grade and used without further purification. Commercial nickel foam (NF) is purchased from Changsha Lyrun New Material Co.

S1.2 Syntheses of the [$La_xFe_{1-x}(H_2O)_8Fe(CN)_6$]·2hmt precursors

The synthesis of [$La(H_2O)_8Fe(CN)_6$]·2hmt is according to the work reported previously [1]. The typical procedure is as follows: $K_3[Fe(CN)_6]$ (1 mmol, 329 mg), $La(NO_3)_3 \cdot 6H_2O$ (1 mmol, 433 mg), $Fe(NO_3)_3 \cdot 9H_2O$ (1 mmol, 404 mg), hmt (2 mmol, 280 mg) were mixed with a molar ratio of 1: 1: 1: 2 in 20 mL deionized water, then stirred under room temperature overnight. The obtained precipitation was centrifuged and washed by deionized water and ethanol for three times, then was dried in an oven at 60 °C overnight.

[$La_{0.5}Fe_{0.5}(H_2O)_8Fe(CN)_6$]·2hmt was synthesized under similar condition as described above except that 1 mmol $La(NO_3)_3 \cdot 6H_2O$ was replaced by 0.5 mmol $La(NO_3)_3 \cdot 6H_2O$ and 0.5 mmol $Fe(NO_3)_3 \cdot 9H_2O$.

Similarly, in the preparation of [$La_{0.33}Fe_{0.67}(H_2O)_8Fe(CN)_6$]·2hmt, 0.33 mmol $La(NO_3)_3 \cdot 6H_2O$ and 0.67 mmol $Fe(NO_3)_3 \cdot 9H_2O$ were utilized instead of 1 mmol $La(NO_3)_3 \cdot 6H_2O$. And a free-La precursor was also synthesized for comparison, in which 1 mmol $La(NO_3)_3 \cdot 6H_2O$ was completely replaced by 1 mmol $Fe(NO_3)_3 \cdot 9H_2O$.

S1.2 Syntheses of La-doped FeS_2/NC and FeS_2/NC

La-doped FeS_2/NC and FeS_2/NC were synthesized by annealing the above precursors in the presence of sulfur. The procedure is as follows: 100 mg of the as-prepared precursor and 1.4 g of sulfur powder were placed in two porcelain boats, and the porcelain boat with sulfur was located on the upstream side of tubular furnace. Then the precursor was heated at 400 °C for 1 hour in N_2 atmosphere with a heating rate of 5 °C per minute. The annealed products of the $[La_{0.5}Fe_{0.5}(H_2O)_8Fe(CN)_6]\cdot 2hmt$, $[La_{0.33}Fe_{0.67}(H_2O)_8Fe(CN)_6]\cdot 2hmt$ and the free-La precursors are designated as La-doped FeS_2/NC-0.5, La-doped FeS_2/NC-0.33 and FeS_2/NC, respectively.

S1.3 Structural characterizations

The X-ray diffraction (XRD) data of all the samples were obtained by using the Tongda TD-3500 Diffractometer with Cu Kα radiation ($\lambda = 1.54056$ Å). The metallic elemental contents were determined by inductively coupled plasma atomic emission spectroscopy (ICP GREEN, SPECTRO) with the wavelength range of 163 - 770 nm. Raman spectra were collected on a Renishaw invia Raman spectrometer with a laser wavelength of 514.5 nm as the excitation source and with a laser output power of 2 mW. The morphologies and micro-structures of the samples were observed by a Quattro S field-emission scanning electron microscopy (SEM) and a JEOL JEM-2100F transmission electron microscopy (TEM). Elemental mappings were analyzed by energy dispersive X-ray spectroscopy (EDS) with the AMETEK spectrometer (USA) attached to Quattro S SEM. Thermogravimetric (TG) curve was measured using the Netzsch STA 449F3 instrument in N_2 atmosphere with a ramp rate of 14 °C min^{-1}. The chemical compositions and valence states of the samples were examined by X-ray photoelectron spectroscopy (XPS) (Escalab 250XI) with Al Kα X-ray as an excitation source, and the data was calibrated according to the standard C-peak binding energy (286.4 eV). The specific surface area and pore size distribution of the material were analyzed by nitrogen adsorption/desorption at ultra-low temperature of 77 K.

S1.4 Electrochemical measurements

Electrochemical measurements were conducted on an electrochemical workstation (CHI660E) in a 1 M KOH solution with a standard three-electrode system, in which Hg/HgO electrode acted as the reference electrode, while the 1 cm × 1 cm platinum plate served as the counter electrode, and the sample-modified Ni foam (NF) was used as the working electrode. The preparation of working electrode was as follows: 2 mg sample was dispersed in 1 mL ethanol with 50 μL of Nafion solution (5 wt %, Sigma-Aldrich) under ultrasonication to form a homogeneous ink, then was drop-coated and pasted on a Ni foam (1×1 cm^2) dried at 60°C in an oven. Before the electrochemical measurements, the samples were electrochemically preactivated by dozens of cyclic voltammetric (CV) scans at a scan rate of 150 mV s^{-1}. After that, oxygen evolution reaction (OER) polarization curves, including linear sweep voltammetry (LSV) and Tafel plot, were recorded from 0.924 to 1.674 V vs RHE at a scanning rate of 2 mV s^{-1} at room temperature to evaluate the catalytic performance of the samples. All the obtained potential values are not iR-corrected and converted to the reversible hydrogen electrode (RHE) reference scale based on E(vs RHE) = E(vs Hg/HgO) + 0.098 + 0.059V × pH, and all the current densities (mA cm^{-2}) have been normalized relative to 1 mg of the sample loading. The electrochemical activity area (ECSA) was estimated by CVs at different sweep rates in the potential range of 0.90 V-1.00 V vs RHE. Electrochemical impedance (EIS) was measured at 1.57 V vs RHE in the frequency range of 0.01-10^5 Hz with an amplitude of 5 mV. The long-term durability was evaluated by chronopotentiometry test, which was carried out at a current density of 20 mA cm^{-2} for 60 h.

S1.5 Density functional theory (DFT) calculations

The DFT calculations were performed in the Vienna ab initio simulation package within a general gradient approximation (GGA) parametrized by projector augmented wave (PAW) pseudopotentials and Perdew-Burke-Ernzerhof (PBE) exchange correlation functional [2, 3]. The ionic forces were converged within 0.05 eV $Å^{-1}$, the convergence threshold for the total energy was 10^{-5} eV, while a plane-wave energy cut-off was set as 400 eV. The Brillouin zone was sampled with a 4 × 4 × 4 Monkhorst-Pack k-point mesh. Based on the crystallographical data of FeS_2 (ICSD No. 53529), a La-doped FeS_2 (200) slab with a thickness of three layers is built in comparison with an undoped FeS_2 (200) slab to calculate density of states (DOS) and the interaction between adsorbate and catalyst. The atoms in the top layer were relaxed, while the middle and bottom layers were fixed. The vacuum space was 20 Å to avoid any artificial effect.

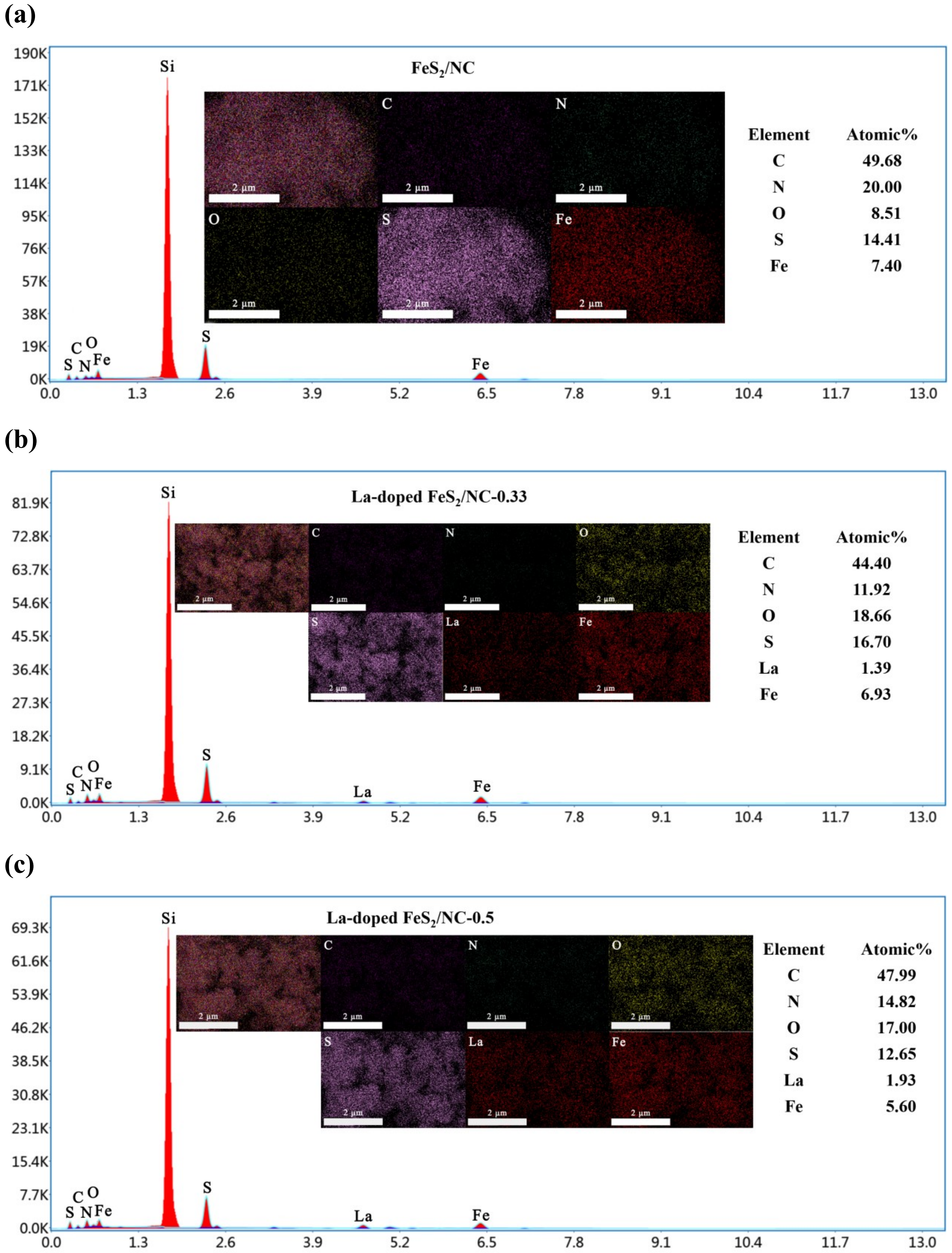

Element	Atomic%
C	49.68
N	20.00
O	8.51
S	14.41
Fe	7.40

Element	Atomic%
C	44.40
N	11.92
O	18.66
S	16.70
La	1.39
Fe	6.93

Element	Atomic%
C	47.99
N	14.82
O	17.00
S	12.65
La	1.93
Fe	5.60

Fig. S1 EDS and elemental mappings of (**a**) FeS$_2$/NC, (**b**) La-doped FeS$_2$/NC-0.33 and (**c**) La-doped FeS$_2$/NC-0.5.

Table S1 The element contents of La and Fe in La-doped FeS_2/NC-0.33 and La-doped FeS_2/NC-0.5.

Sample	Element	μg mL^{-1}	μmol mL^{-1}
La-doped FeS_2/NC-0.33	La	10.7	0.077
	Fe	15.6	0.279
La-doped FeS_2/NC-0.5	La	13.3	0.096
	Fe	12.8	0.229

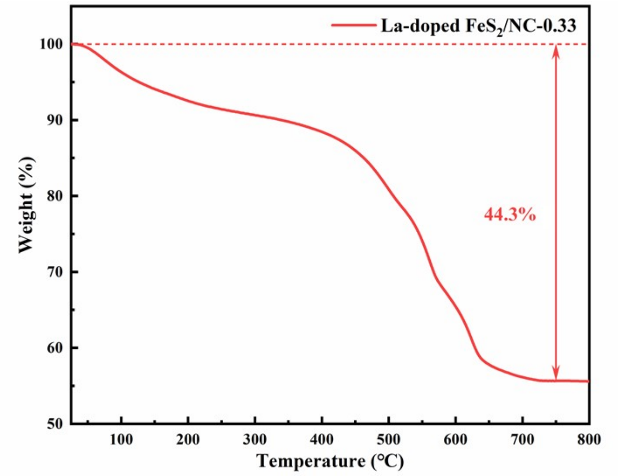

Fig. S2 TG curve of La-doped FeS_2/NC-0.33.

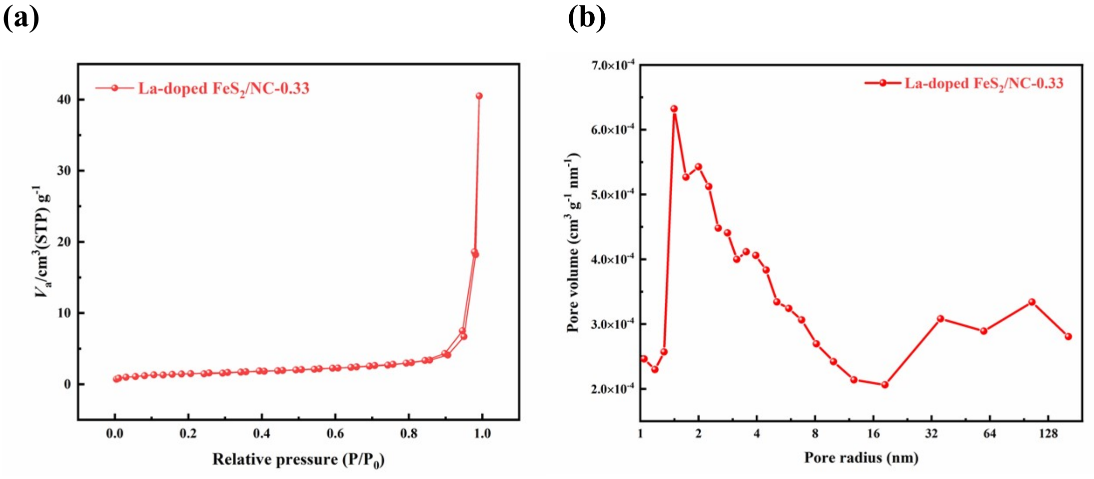

Fig. S3 (**a**) Nitrogen adsorption/desorption isotherms and (**b**) pore-size distribution of La-doped FeS_2/NC-0.33.

Table S2 Comparison of OER performances of different iron sulfide-based catalysts

Catalyst	Overpotential (mV) @ current density (mA cm^{-2})	Tafel slope (mV dec^{-1})	Electrolyte	Reference
La-doped FeS_2/NC-0.33	139@10	54	1 M KOH	**This work**
FeS_2/TiO_2	590@10	48.8	0.1 M KOH	[4]
FeS_2CL@WS_2NS	260@10	54	1 M KOH	[5]
FeS_2@MXene	240@10	58.7	1 M KOH	[6]
Ni-FeS_2-0.5	250@10	34	1 M KOH	[7]
FeS_2/C	350@10	65.6	1 M KOH	[8]
Co–FeS_2/CoS_2	278@10	73	1 M KOH	[9]
Fe_3O_4/FeS_2-2.5	253@10	48	1 M KOH	[10]
FeS_2/TiO_2	230@100	47	1 M KOH	[11]
FeS_2-MoS_2@CoS_2-MOF	211@20	64.5	1 M KOH	[12]
FeS_2	189.5@10	71	1 M KOH	[13]
$Co_{0.6}Fe_{0.4}S_2$@N-CNTs/rGO	248@10	58.3	1 M KOH	[14]
FeS_2/MCoNiSe_2/NF	230@10	54.1	1 M KOH	[15]
CoS_2–FeS_2	210@10	46	1 M KOH	[16]
Fe_3O_4/FeS_2-2.5	253@10	48	1 M KOH	[17]
$Co_{0.25}Fe_{0.75}S_2$	324@10	50	1 M KOH	[18]

Table S3 The values for the parameters in the simulated equivalent circuit for La-doped FeS_2/NC-0.33 before and after 60h-electrolysis and FeS_2/NC.

Sample	R_s (Ω cm^{-2})	R_{ct} (Ω cm^{-2})	CPE-T	CPE-P
La-doped FeS_2/NC-0.33	1.571	0.257	0.029724	0.7139
La-doped FeS_2/NC-0.33 after 60 h-electrolysis	1.502	0.283	0.026546	0.7538
FeS_2/NC	3.136	0.872	0.023389	0.7071

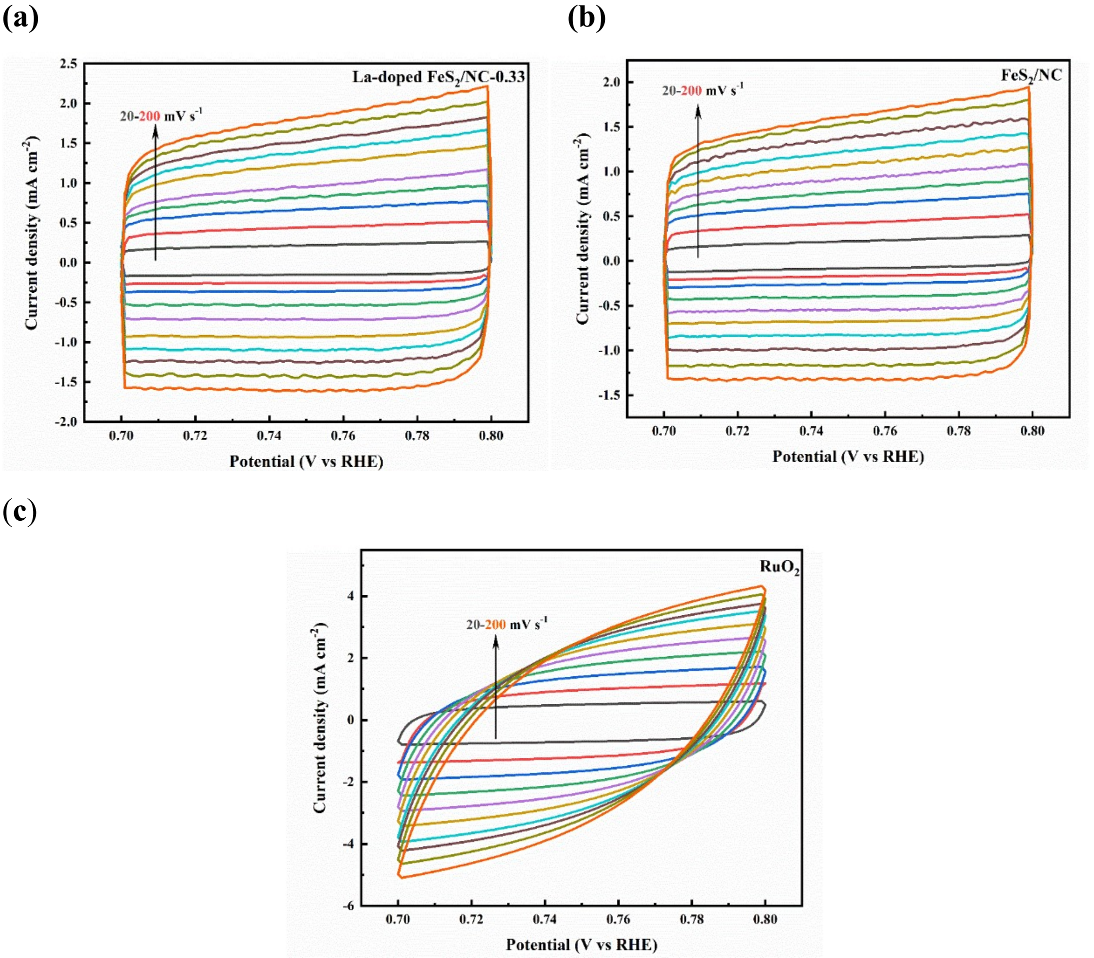

Fig. S4 CV curves of (**a**) La-doped FeS_2/NC-0.33, (**b**) FeS_2/NC and (**c**) RuO_2 measured in 1 M KOH solution at different scan rates of 20 to 200 mV s^{-1}.

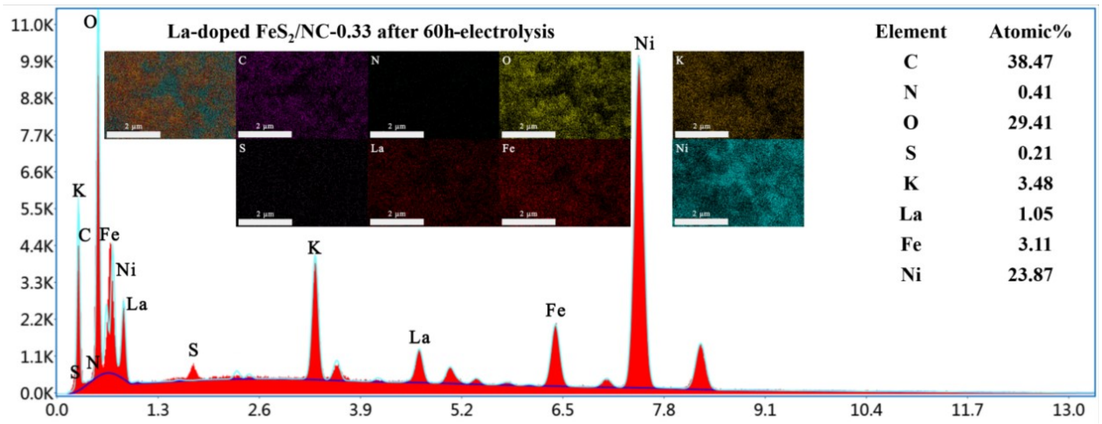

Element	Atomic%
C	38.47
N	0.41
O	29.41
S	0.21
K	3.48
La	1.05
Fe	3.11
Ni	23.87

Fig. S5 EDS and elemental mappings for La-doped FeS$_2$/NC-0.33 after 60 h-electrolysis.

Table S4 The DFT calculation results for La-doped FeS$_2$ and FeS$_2$.

	La-doped FeS$_2$	FeS$_2$
$\triangle G_{\text{M-OH*}}$ (eV)	-0.041	0.859
$\triangle G_{\text{M-O*}}$ (eV)	0.081	1.128
$\triangle G_{\text{M-OOH*}}$ (eV)	1.708	2.700
$\triangle G_1$ (eV)	0.792	1.692
$\triangle G_2$ (eV)	0.955	1.102
$\triangle G_3$ (eV)	2.460	2.405
$\triangle G_4$ (eV)	4.045	3.053

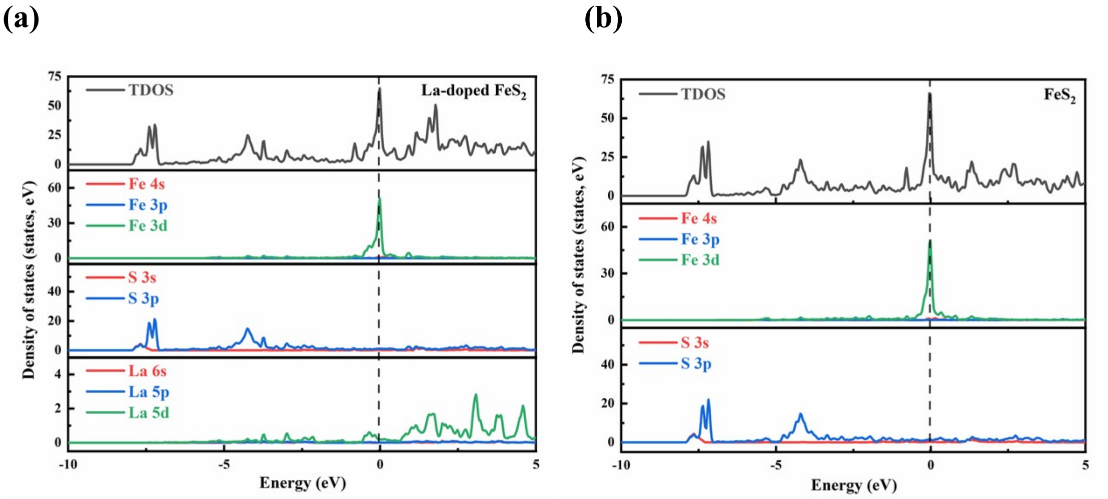

Fig. S6 Total and Partial DOS for (**a**) La-doped FeS$_2$ and (**b**) FeS$_2$, in which s, p and d orbitals are denoted in blue, red and green, respectively. The position of the Fermi level is indicated by a black dotted vertical line at 0 eV.

Reference:

[1] S. A. Stoian, C. Paraschiv, N. Kiritsakas, F. Lloret, E. Münck, E. L. Bominaar, and M. Andruh, Mössbauer, electron paramagnetic resonance, and magnetic susceptibility studies on members of a new family of cyano-bridged 3d-4f complexes. Demonstration of anisotropic exchange in a Fe-Gd complex, Inorg. Chem. 49 (2010) 3387-3401.

[2] J. P. Perdew, K. Burke and M. Ernzerhof, Generalized gradient approximation made simple, Phys. Rev. Lett. 77 (1996) 3865-3868.

[3] P. E. Blochl, Projector augmented-wave method, Phys. Rev. B 50 (1994) 17953-17979.

[4] P. Pandey, S. Gahlawat, and P. P. Ingole, Physical barricading at the nanoscale: Protecting pyrite from weathering toward efficient and stable electrocatalysis of the oxygen evolution reaction, ACS Sustain. Chem. Eng. 8 (2020) 15584-15594.

[5] G. T. Zhang, Z. T. Hao, J. Yin, C. Wang, J. H. Zhang, Z. Y. Zhao, D. H. Wei, H. W. Zhou and Z. C. Li, FeS_2 crystal lattice promotes the nanostructure and enhances the electrocatalytic performance of WS_2 nanosheets for the oxygen evolution reaction, Dalton Trans. 49 (2020) 9804.

[6] Y. Y. Xie, H. Z. Yu, L. M. Deng, R. S. Amin, D. S. Yu, A. E. Fetohi, M. Y. Maximov, L. L. Li, K. M. El-Khatib and S. J. Peng, Anchoring stable FeS_2 nanoparticles on MXene nanosheets via interface engineering for efficient water splitting, Inorg. Chem. Front. 9 (2022) 662.

[7] Z. Tan, L. Sharma, R. Kakkar, T. Meng, Y. Jiang, and M. H. Cao, Arousing the reactive Fe Sites in pyrite (FeS_2) via integration of electronic structure reconfiguration and in situ electrochemical topotactic transformation for highly efficient oxygen evolution reaction, Inorg. Chem. 58 (2019) 7615-7627.

[8] K. F. Pan, Y. Y. Zhai, J. W. Zhang and K. Yu, FeS_2/C nanowires as an effective catalyst for oxygen evolution reaction by electrolytic water splitting, Materials 12 (2019) 3364.

[9] K. Wang, W. L. Guo, S. C. Yan, H. Z. Song and Y. Shi, Hierarchical Co–FeS_2/CoS_2 heterostructures as a superior bifunctional electrocatalyst, RSC Adv. 8 (2018) 28684.

[10] M. J. Wang, X. Q. Zheng, L. L. Song, X. Feng, Q. Liao, J. Li, L. Li and Z. D. Wei, Fe_3O_4/FeS_2 heterostructures enable efficient oxygen evolution reaction, J. Mater. Chem. A 8 (2020) 14145.

[11] Z. J. Chen, R. J. Zheng, S. M. Deng, W. F. Wei, W. Wei, B. J. Ni and H. Chen, Modular design of an efficient heterostructured FeS_2/TiO_2 oxygen evolution electrocatalyst via sulfidation of natural ilmenites, J. Mater. Chem. A 9 (2021) 25032.

[12] K. Chhetri, A. Muthurasu, B. Dahal, T. Kim, T. Mukhiya, S. H. Chae, T. H. Ko, Y. C. Choi, H.Y. Kim, Engineering the abundant heterointerfaces of integrated bimetallic sulfide-coupled 2D MOF-derived mesoporous CoS_2 nanoarray hybrids for electrocatalytic water splitting, Mater. Today Nano 17 (2022) 100146.

[13] G. Z. Wang, C. Y. Jin, G. T. Zhang, L. J. Qian, X. Chen, J. F. Tan, W. H. Wang, J. Yin, X Liu, and H. W. Zhou, Surface self-reconstructed amorphous/crystalline hybrid iron disulfide for high-efficiency water oxidation electrocatalysis, Dalton Trans. 50 (2021) 6333.

[14] Z. L. Zhang, D. Y. Xua, J. H. Li, J. L. Liu, X. D. Long, K. D. Su, J. N. Guo, H. X. Tong, Z. Liu, D. Qian, Highly electrocatalytic performance of bimetallic Co-Fe sulfide nanoparticles encapsulated in N-doped carbon nanotubes on reduced graphene oxide for oxygen evolution, J. Alloys Compd. 881 (2021) 160667.

[15] J. L. Yang, H. C. Xuan, J. T. Yang, L. X. Meng, J. Wang, X. H. Liang, Y. P. Li, P. D. Han, Metal-organic framework-derived $FeS_2/CoNiSe_2$ heterostructure nanosheets for highly-efficient oxygen evolution reaction, Appl. Surf. Sci. 578 (2022) 152016.

[16] W. P. Wang, Y. Xu, J. L. Yao, X. E. Liu, Z. M. Yin and Z. C. Li, Enhanced oxygen and hydrogen evolution performance by carbon-coated CoS_2-FeS_2 nanosheets, Dalton Trans. 49 (2020) 13352-13358.

[17] M. J. Wang, X. Q. Zheng, L. L. Song, X. Feng, Q. Liao, J. Li, L. Li and Z. D. Wei, Fe_3O_4/FeS_2 heterostructures enable efficient oxygen evolution reaction, J Mater Chem A 8 (2020) 14145-14151.

[18] L. F. Gao, C. Y. Guo, X. J. Liu, X. J. Ma, M. Z. Zhao, X. Kuang, H. Yang, X. J. Zhu, X. Sun and Q. Wei, Co-Doped FeS_2 with a porous structure for efficient electrocatalytic overall water splitting, New J. Chem. 44 (2020) 1711.